Understanding the Black Hole Shadow of M87 with Wald's Solution

Raoul Emanuel Kinadeter

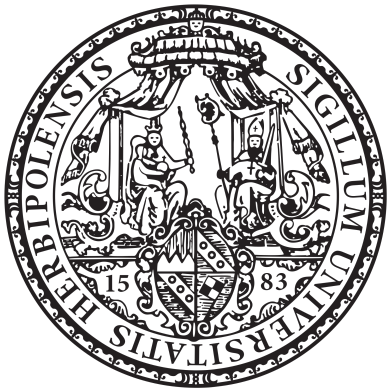

Bachelorarbeit

Institut für Theoretische Physik
und Astrophysik
Lehrstuhl für Astronomie
Julius-Maximilians-Universität Würzburg

Betreuer: Prof. Dr. Karl Mannheim

Würzburg, den 05.05.2020

Contents

List of Figures

Abstract

The image of the black hole shadow of M87 provided the first direct evidence of the existence of black holes in 2019. The EHT collaboration interpreted the bright emission ring as the photon sphere, which is created by the presence of a supermassive black hole. The radiation supposedly comes from mm-synchrotron radiation of electrons in the accretion disk. In this thesis we give an alternative explanation for the origin of the emission ring. We examine how a similar morphology can be due to the synchrotron emission of relativistic electrons in M87's jet inside the black hole magnetosphere, as described by Robert Wald. In order to do this, we calculate and discuss the surfaces of constant magnetic flux inside the rotating Kerr-spacetime and study the emitted synchrotron power of electrons in the resulting magnetic field.

Das Bild des Schattens des Schwarzen Loches von M87 lieferte 2019 den ersten direkten Nachweis über die Existenz Schwarzer Löcher. Die EHT Kollaboration interpretierte den hellen Emissionsring als Photonensphäre, die durch die Anwesenheit eines supermassiven Schwarzen Loches entsteht. Die Strahlung sei mm-Synchrotronstrahlung von Elektronen in der Akkretionsscheibe. In dieser Arbeit wird eine alternative Erklärung für den Ursprung des Emissionsringes aufgezeigt. Wir erklären, wie eine ähnliche Morphologie durch Synchrotronstrahlung relativistischer Elektronen im Jet von M87 in der Magnetosphäre des Schwarzen Loches, die von Robert Wald beschrieben wurde, zustande kommen kann. Dazu berechnen wir die Flächen konstanten magnetischen Flusses in der rotierenden Kerr-Raumzeit und untersuchen die emittierte Synchrotronleistung von Elektronen im resultierenden Magnetfeld.

1 M87 and the Black Hole Image

In this chapter we will discuss the radio galaxy M87 in general, explore the EHT collaboration and explain the famous image of M87's central black hole.

1.1 Overview

The object Messier 87, or M87, is a giant elliptical galaxy in the constellation of Virgo and member of the Virgo galaxy cluster (Fig. 1) about 16.7 Mpc [18] from our solar system. It hosts an Active Galactic Nucleus (AGN) and possesses a jet of outflowing matter. This is one of the reasons why M87 is called an active galaxy. Active galaxies have a high bolometric luminosity that emerges from a relatively small region around their center and can not be explained by or associated with star light or star formation. The high luminosities can only be explained by a matter accreting central super massive black hole. In case of M87 the black hole M87* has a mass of $M_{BH} = 6.5 \cdot 10^9 \, M_\odot$, with the solar mass $M_\odot$ and a bolometric luminosity of about $L_{bol} \approx 2.7 \cdot 10^{42} \frac{ers}{s}$ [18].

Figure 1: The elliptical galaxy M87
An infrared/visible composite picture. [26]
The jet extends at least 4900 light years into space [28].

AGN can be classified with the help of the AGN Unified Model. According to the Unified Model the structure of the central region of an AGN is as follows (see Fig.2): At the very core sits the super massive black hole. It is surrounded by an accretion disk of matter (plasma, gas, dust, etc.). The region up to about 0.1pc is called the broad line region (BLR) because emission lines in the AGN spectra are broadened due to the high velocities in the close vicinity around the black hole by Doppler broadening. At about $1 - 10$pc an opaque torus of gas and dust contains the accretion region. The torus is one of the reasons for the multitude of different types of AGN, as we will see. Finally, we have the narrow line region (NLR), which contains ionized clouds of gas and lies about $10 - 100$pc from the central black hole. The spectral lines from this region are relatively narrow compared to the BLR, since the velocities at these distances are much smaller. Additionally, the AGN can have a jet, which would classify it as radio-loud. Otherwise, the AGN is called radio-quiet.
The different types of AGN can be explained by this model, if we consider the viewing

angle of the observer relative to the torus.
Let us illustrate this at the example of Seyfert 1 and Seyfert 2 galaxies (see also Fig.2). The spectra of Seyfert 2 galaxies only contains narrow emission lines, whereas those of Seyfert 1 also contain broad emission lines. According to the Unified Model this is due to the fact that the observer views the Seyfert 2 galaxy close to the plane in which the torus resides. The torus blocks the view into the broad line region. Contrarily, a Seyfert 1 galaxy is viewed more from the top, closer to the rotation axis of the accretion disk. From here, the view into the BLR is clear, thus explaining the different spectral features.
In case of M87, the angle between the jet and our line of sight amounts to $\approx 17°$ [37]. So we look at the accretion disk almost directly from the top. This classifies M87 as a blazar, according to the Unified Model. M87 is also referred to as a low-luminosity AGN (LLAGN) due to its relatively low accretion rate, compared to the Eddington limit [15]. The Eddington luminosity is the 'extreme' case, where the energy, gained by matter accretion, is completely released into radiation.

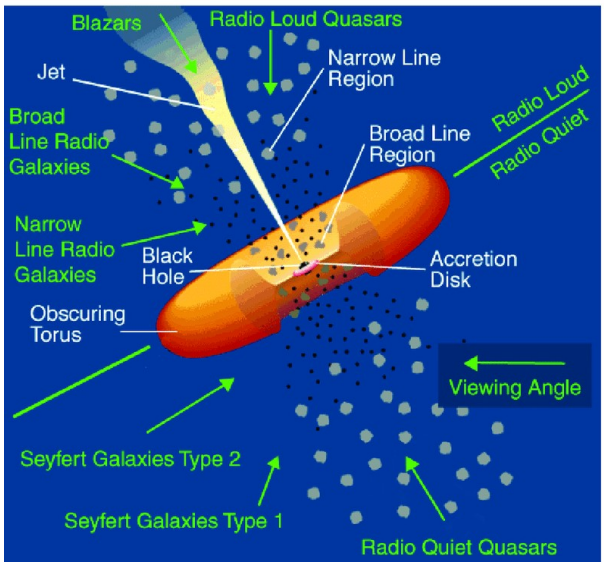

Figure 2: The AGN Unified Model
Structure of the central region in the AGN Unified Model. The different parts of the AGN are labeled in white; the resulting types of AGN are depicted in green. [30]

1.2 The EHT Collaboration

The EHT collaboration consists of over 300 scientists from more than 20 countries [8]. It was formed with the intent to image the immediate vicinity of the black holes M87* and SgrA*, the black hole at the center of the Milky Way.
The high angular resolution required to accomplish this objective can be achieved by using Very Long Baseline Interferometry (VLBI). Mathematically the resolution of a telescope is dependent on the telescope's dish size D and the observation wavelength λ via

$$R \sim \frac{\lambda}{D},$$

so a large dish size is desired at small wavelengths. The VLBI technique allows for multiple radio telescopes all over the globe to be connected into a giant virtual telescope with a 'dish' of about the size of earth's diameter. D is given here by the maximum length of the baseline between two telescopes in the array. EHT operates at a wavelength of $\lambda = 1.33\,\text{mm}$ but this came with major technical challenges, since reducing the observation wavelength introduces noise and atmospheric disturbances. After several years of improvement, the EHT team finally reached a theoretical, diffraction-limited resolution of $\approx 25\,\mu$as ([1] Sec. 3).
In order to produce an image from the measured EHT data, the scientists had to face another challenge. The telescopes within the array are located at only six locations around the earth so there are a lot of 'gaps', missing pieces of information to accurately reconstruct the image. In [8] this is compared to sound and music. Humans are able to recognize a piece of music even when several notes, required to play the song, are missing. Our brain is able to fill in the missing information. In imaging this filling in of missing information is done by the complex imaging algorithms, developed by the EHT team, which can single out one or several images, depending on how likely they are to be accurate [9]. These 'gaps' are addressed by the term 'uv-coverage'. The uv-plane is the 'Fourier' plane of spatial frequencies that the interferometer samples. u and v are the conjugated coordinates of the true spatial coordinates x and y in the image plane. They measure the distance between wave fronts. Due to earth's rotation the projected baselines between telescope sites trace out an arc in the (u, v)-plane (see Fig.3). From the point of view of a distant object (e.g. a star) a north-south baseline seems to rotate, whereas an east-west baseline seems to grow and shrink (and slightly rotate). The points in the uv-plane can then be mapped onto the actual image in the sky by a Fourier transformation. The more telescopes there are in the array, the higher the uv-coverage. This leads to better image reconstruction. Longer baselines grant a higher angular resolution. [8]

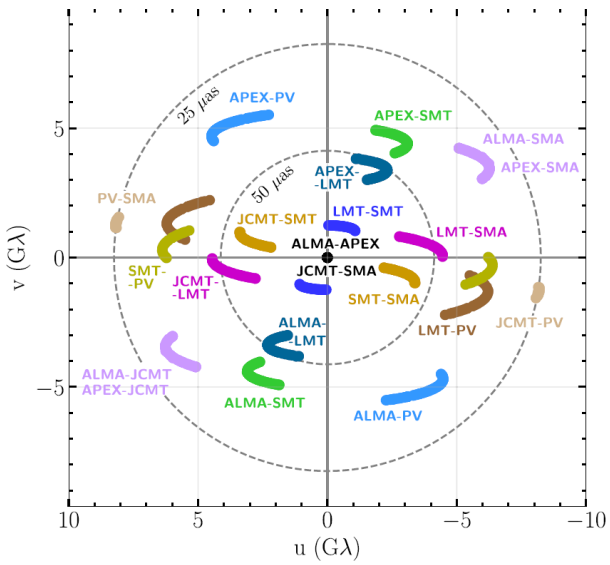

Figure 3: uv-coverage
uv-coverage of EHT for the M87* observation that produced the final black hole image. [1]

With the captured data, the EHT scientists measured the following properties, among others, of M87*:

- Mass: $M = (6.5 \pm 0.7)10^9\,\mathrm{M}_\odot$
- Ring diameter: $42 \pm 3\,\mu$as
- Gravitational radius: $r_g = 3.8 \pm 0.4\,\mu$as
- Black hole rotation: clockwise, as seen from earth (angular momentum vector points away from earth)

1.3 The Black Hole Image

Figure 4: The black hole image of M87
The black hole shadow surrounded by an asymmetric bright emission ring. [8]

Now, let us discuss the actual image of M87* (Fig.4). It shows a bright ring with a diameter of $42 \pm 3\,\mu$as [1] that contains the dark black hole 'shadow'. Let us first focus on the shadow.
To understand the central dark region, we need to know about the concept of the photon sphere. To explain this, we will consider the simple case of a non-rotating Schwarzschild black hole (see Sec. 2.1.1).
In the framework of General Relativity, one can calculate the stable orbits of photons around a black hole, by solving the light-like geodesics of the Schwarzschild metric. One finds that there is a particular distance from the black hole at $r_P = \frac{3}{2} r_S = \frac{3MG}{2c^2}$, where photons are bound to the black hole in unstable orbits [29]. r_S is called the Schwarzschild radius and marks the black hole horizon (see Sec.2.1.1). If an observer far away from the black hole observes light from a remote source that is reflected off a black hole, there is an effective potential $V(r)$ for the photon trajectory, similar to classical mechanics, which is related to the impact parameter b and is given by

$$V(r) = \frac{1}{r^2}\left(1 - \frac{2MG}{rc^2}\right).$$

In order for a photon with impact parameter b to be detectable at a distance r the condition $b \leq V(r)^{-\frac{1}{2}}$ must be met. $V(r)$ has a maximum at $r = r_P = \frac{3MG}{2c^2}$, the photon radius. The value of $V(r)$ at this radius is given by

$$V(r_P) = \frac{1}{27M^2}$$

and therefore we obtain a critical impact parameter $b_c = \sqrt{27}M$. [19] So for distant (infinity) observers the photon radius is rather given by $r_P = b_C = \sqrt{27}M$ [1]. This is illustrated nicely in figure 5. If a photon approaches the black hole with an impact

parameter $b > r_P$, it can escape to infinity. For $b < r_L$ it vanishes into the black hole. And for $b = r_L$ it is bound to an unstable orbit. These photons produce the ring that we can see in figure (1).
In the case of a rotating Kerr black hole (see Sec.(2.1.2)) the treatment becomes a lot more difficult and additionally r_P will depend on the orientation of the incident photon relative to the black hole's angular momentum vector and its cross section. [1]

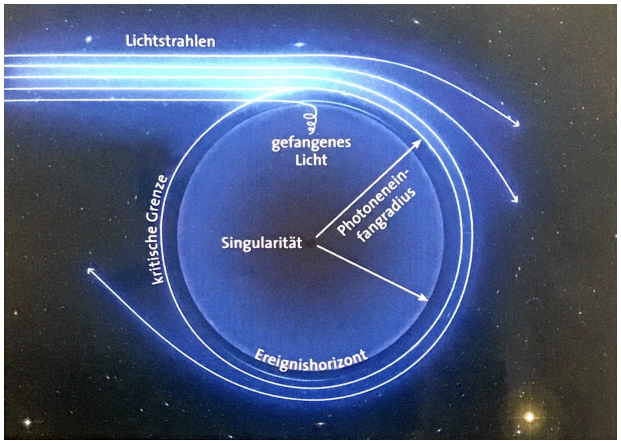

Figure 5: Photon sphere
Photon sphere of a non-rotating black hole (Singularität, Ereignishorizont). Light that has a smaller impact parameter b than the capture radius r_L (Photoneneinfangradius) plunges into the black hole, while it can escape, if $b > r_L$. For $b = r_L$ (kritische Grenze) photons orbit the black hole and create the photon sphere [6]

Now that we have identified the two components and understood their origin, we can take another step and study the photon ring in more detail. So far we have not mentioned the asymmetric shape of the ring, which appears much brighter in the bottom region than at the top. This asymmetry is attributed to relativistic beaming or Doppler beaming [1].
In order to understand the effect of relativistic beaming, let us consider a different feature of the M87 galaxy, its jet (Fig.1), and hit two birds with one stone.
A jet is a stream of matter (electrons, protons, plasma) that is violently ejected from the core region of the galaxy into the galactic, and oftentimes inter-galactic space at relativistic speeds (relativistic jet, extragalactic jet). The exact powering mechanism behind jets are still largely unknown and subject to active research, however, there are two main approaches that try to explain the phenomenon. In the first model, the black hole magnetosphere in the rotating Kerr-space-time (Sec. 2.1.2) powers the jet by extracting rotational energy from the black hole. This is called the Blandford-Znajek mechanism [4], which is closely related to the Magnetic Penrose Process (MPP) [35]. In the second mechanism, named after Blandford and Payne, the magnetosphere extracts rotational energy from the accretion disk [3]. Jets have been suggested to take a main part in par-

ticle acceleration and the origin of ultra-high-energy cosmic rays (UHECRs). [33]
So what does this have to do with relativistic beaming? In fact, there should be two jets. According to the AGN Unified Model there is a second 'counter jet' on the opposite side. However, we can not see the counter jet in Fig. 1.

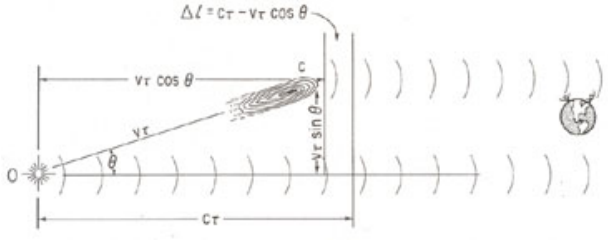

Figure 6: Sketch for the apparent superluminal motion of an extragalactic jet [27]

Consider the following situation (Fig.6) [27]: The jet originates from a point O and travels towards the earth at an angle θ at relativistic speeds close to the speed of light $v_J <\approx c$. If we measure the electromagnetic waves (usually synchrotron radiation) that the jet emitted at O, that radiation covered a distance ct in a certain time t. The jet travels a distance $\Delta x_{\parallel} = v_J t cos\theta$ directly toward the earth and a distance $\Delta x_{\perp} = v_J t sin\theta$ perpendicular to that direction. Radiation that reaches us from the new position of the jet is delayed by a time interval

$$\Delta t = t\left(1 - \underbrace{\frac{v_J}{c}}_{=\beta_J} cos\theta\right).$$

From earth, the apparent velocity perpendicular to the line of sight is

$$v_{app} = \frac{\Delta x_{\perp}}{\Delta t} = \frac{v_J sin\theta}{(1 - \beta cos\theta)}.$$

For relativistic jet velocities v_J, which we assumed, and small viewing angles θ, v_{app} can be several times greater than the speed of light. This effect is called (apparent) superluminal motion.
The jet in the direction of the observer ($\theta \approx 0$) and the counter jet ($\theta \approx \pi$) can be described by a modified Doppler factor

$$\delta_J = \frac{1}{\gamma_J}(1 - \beta_J cos\theta)^{-1}$$

For a standard synchrotron power law spectrum with spectral index α

$$f_\nu \sim \nu^\alpha$$

The Doppler beaming now leads to an increased/decreased apparent brightness by a factor

$$f_{\nu,app} = f_\nu \delta_J^{3-\alpha}.$$

So the observed brightness of the approaching jet is multiplied and outshines the much fainter light of the counter jet, which is consequentially no longer visible. ([21] pp. 26-28)

As stated above, M87's jet is about 17° off the line of sight from earth. So we are looking at the accretion plane from an angle, where the southern side is slightly closer to earth. Additionally, the accretion disk rotates clockwise, which means the southern side approaches earth, while the north spins away from us. Thus, the southern side of the photon ring is beamed in the same way as described above, making the ring appear brighter in the south and darker in the north. The resulting image is consistent with a rotating Kerr black hole. [10]

1.4 Goal

We have described that the ring-like morphology observed with the mm-VLBI technique of M87 can be explained by the presence of a photon sphere associated with a supermassive black hole, as detailed by the EHT Collaboration. The basic assumption of this explanation is that the electrons in the accretion flow of M87 are spontaneously heated up to the kinetic temperature of virialized ions which, is much higher than that of electrons due to radiative losses, leading to quasi-thermal mm-cyclotron emission. By contrast, the radio emission of M87 at longer wavelengths seems to be dominated by the non-thermal synchrotron emission of relativistic electrons accelerated by plasma processes in the jet [1]. Therefore, in this thesis, our objective is to address the problem if the observed ring-like morphology could in fact be due to anisotropic synchrotron emission of relativistic electrons in the curved magnetic field at the base of the jet near the supermassive black hole. Such electrons could arise due to the acceleration in field-parallel electric fields across vacuum gaps, as known from pulsar physics [17]. As a simple toy model for the topology of the magnetic field advected by the accretion flow, we study Robert Wald's solution for a rotating Kerr black hole immersed in an external uniform magnetic field and consider the resulting distribution of pitch angles of electrons assumed to be accelerated in the direction of the jet along the spin axis of the black hole and their corresponding synchrotron photon flux.

2 Wald's Solution

Before we can start the discussion of Wald's solution, we may want to review some basics of Einstein's theory of General Relativity.

2.1 Overview of General Relativity

One of the central pillars of General Relativity are Einstein's field equations, which describe how space-time is bent by matter. 'Matter' here meaning 'anything but gravity', i.e. matter, charges and radiation, which are not gravitational in nature.
The equations can be derived from a calculation of variations of the principle of least action with the help of the heuristic principle of simplicity, where one applies the ansatz that the total action of the universe can be expressed by the sum of a gravitational term and another term related to the matter: $S = S_G + S_M$. In their final form Einstein's field equations read:

$$R_{\mu\nu} - \frac{1}{2}Rg_{\mu\nu} + \Lambda g_{\mu\nu} = \frac{8\pi G}{c^4}T_{\mu\nu}. \tag{1}$$

Here $g_{\mu\nu}$ is the space-time metric tensor and Λ the cosmological constant. $R_{\mu\nu}$ denotes the Ricci tensor, R the Ricci scalar and $T_{\mu\nu}$ is the energy-momentum tensor, which represents the matter distribution.
The Ricci tensor is defined in terms of the Riemann curvature tensor by contracting the latter's first and third indices:

$$R_{\mu\nu} = R^{\rho}_{\mu\rho\nu}, \tag{2}$$

where, as usual $\mu, \nu \in \{0, 1, 2, 3\}$. Because of the symmetry of the Riemann tensor, only 10 out of the 16 components are independent. Therefore, the left-hand side of (1) has to be symmetric as well and only 10 components of $T_{\mu\nu}$ are independent respectively ([12] pp. 122-126).

2.1.1 The Schwarzschild Metric

Now that we have seen the fundamental equations of general relativity, we want to explore them a little deeper by looking at an actual solution. The simplest solution was proposed by Karl Schwarzschild in 1916, shortly after Einstein first published his field equations and stated it would take a long time until someone would be able to solve them.
The Schwarzschild solution describes the gravitational field of a spherical object in vacuum that carries neither charge nor angular momentum. If the object is situated in vacuum, the energy-momentum tensor vanishes, i.e. $T_{\mu\nu} = 0$. The cosmological constant Λ is set to 0 as well. The field equations simplify in this case to

$$R_{\mu\nu} - \frac{1}{2}Rg_{\mu\nu} = 0. \tag{3}$$

These new equations can be solved exactly and the result yields the Schwarzschild metric in spherical coordinates, which is represented by the line element

$$ds^2 = \underbrace{-c^2\left(1-\frac{2GM}{c^2r}\right)}_{g_{tt}}dt^2 + \underbrace{\left(1-\frac{2GM}{c^2r}\right)^{-1}}_{g_{rr}}dr^2 + \underbrace{r^2}_{g_{\theta\theta}}d\theta^2 + \underbrace{r^2sin^2\theta}_{g_{\varphi\varphi}}d\varphi^2. \tag{4}$$

From (4) we can read off several interesting properties. First of all, far away from the object, i.e. $r \to \infty$ the line element simplifies to the Minkowski metric on a sphere:

$$ds^2 = -c^2dt^2 + dr^2 + r^2d\theta^2 + r^2sin^2\theta d\varphi^2. \tag{5}$$

We obtain the very same result for the case of vanishing mass, $M \to 0$. So if the gravitational influence of the mass disappears, the Schwarzschild metric reduces to the Minkowski metric of flat space.
Next, the metric does not explicitly depend on t and φ, which means it is stationary and axisymmetric. Similarly to classical mechanics, where symmetries of the Lagrangian indicated conservation laws, we have Killing vectors in differential geometry to identify these symmetries.
Since the metric is independent of t and φ, this gives rise to the Killing vectors

$$\frac{\partial}{\partial t} \qquad \text{and} \qquad \frac{\partial}{\partial \varphi}. \tag{6}$$

The geometric interpretation is, roughly speaking, if the metric tensor is independent of a coordinate in a given basis, i.e.

$$\frac{\partial g_{\mu\nu}}{\partial x^K} = 0 \tag{7}$$

a curve parameterized by $x^\alpha = c^\alpha(\lambda)$ can be translated in the direction of x^K by $\Delta x^K = \epsilon$ to result in a shifted curve and the lengths of the original and the shifted curves are the same. The object that we measure the length of a curve with, is the metric tensor, so we can say a Killing vector leaves the metric invariant under infinitesimal coordinate changes. In this case we speak of a Killing vector $\xi = \frac{\partial}{\partial x^K}$, which satisfies Killing's

$$\xi_{\mu;\nu} + \xi_{\nu;\mu} = 0, \tag{8}$$

where the semicolon denotes the covariant derivative ([24] pp. 650-651). We will deal with Killing vectors again at a later point.

Finally, the Schwarzschild metric becomes singular for $r = 0$ and

$$r = r_S = \frac{2GM}{c^2}. \tag{9}$$

r_S is called the Schwarzschild radius and marks the event horizon of a Schwarzschild black hole. As we can see, here $g_{tt} \to 0$ and $g_{rr} \to \infty$. It can be shown however, that

the singularity at $r = 0$ is a real singularity in the space-time geometry independent of the chosen coordinates, whereas the one at $r = r_S$ is merely a coordinate-induced singularity and can be avoided by choosing a different coordinate frame, for example Eddington-Finkelstein or Kruskal-Szekeres coordinates. [24] [21]
If we now pass the Schwarzschild radius ($r < r_S$) the term $(1 - \frac{2GM}{c^2 r}) = (1 - \frac{r_S}{r})$ changes its sign, and we end up with the Schwarzschild metric

$$ds^2_{In} = c^2\left(\frac{2GM}{c^2 r} - 1\right)dt^2 - \left(\frac{2GM}{c^2 r} - 1\right)^{-1} dr^2 + r^2 d\theta^2 + r^2 sin^2\theta d\varphi^2. \tag{10}$$

So the temporal component is now positive and the radial distance component has become negative and space and time, roughly speaking, have changed positions. Outside the Schwarzschild radius an observer is bound to always move forward in time. Inside r_S an observer is constrained to move 'forward' toward the central mass M. ([21] pp. 222-224)

> *"This is the essence of a black hole horizon. It is not merely defined by the fact that the escape velocity is the speed of light there. It is that interior to the horizon, time and space are so warped that the future of anything, including light, is predestined to fall into the center."* ([21] p. 224)

To summarize, each massive object has its own Schwarzschild radius, depending on its mass. If the object is contracted to a radius less than r_S, we call that object a black hole.

2.1.2 The Kerr Metric

Now that we have studied the Schwarzschild metric as the simplest solution of Einstein's field equations, and we know what a black hole is, it is time to look at some more general cases.
But before we discuss these, let us take a look at the famous 'No-hair theorem' regarding black holes.
The theorem states that the external gravitational and electromagnetic fields of a stationary black hole are uniquely determined by the black hole's mass M, its charge Q and its intrinsic angular momentum S.
Thus, no further quantities ('hairs') are required to characterize a black hole. ([24] p.876)

When we discussed the Schwarzschild solution in the previous section, one of the assumptions was that the black hole carry neither charge nor angular momentum ($Q = 0$, $S = 0$). There are actually four different vacuum solutions ($T_{\mu\nu} = 0$) depending on these properties:

- Schwarzschild: $S = 0$, $Q = 0$
- Reissner–Nordström: $S = 0$, $Q \neq 0$
- Kerr: $S \neq 0$, $Q = 0$
- Kerr-Newmann: $S \neq 0$, $Q \neq 0$

with the Kerr-Newmann geometry being the most general solution for a rotating and charged black hole.
In this thesis however, it will suffice to focus on the uncharged Kerr solution. The line element in the Boyer-Lindquist coordinates t, r, θ, φ and in natural units ($c = G = 1$) is given by

$$ds^2 = -\left(1-\frac{2Mr}{\Sigma}\right)dt^2+\frac{\Sigma}{\Delta}dr^2+\Sigma d\theta^2+\left(\frac{(r^2+a^2)^2-a^2\Delta sin^2\theta}{\Sigma}\right)sin^2\theta d\varphi^2-\frac{4Marsin^2\theta}{\Sigma}dtd\varphi, \tag{11}$$

where $\Sigma = r^2+a^2cos^2\theta$ and $\Delta = r^2-2Mr+a^2$. "Σ is a radial distance, like r, but surfaces of constant Σ are oblate" ([21] p.234). This is due to the second term, which makes an otherwise circular shape look squashed at the equator. Δ is an expression similar to the Schwarzschild factor in the g_{tt} and g_{rr} components of (4), as we will see below. $a = \frac{S}{M}$ is the angular momentum per unit mass. Another important quantity is the so-called gravitational radius $r_g = \frac{GM}{c^2}$, which is just half a Schwarzschild radius and reduces to $r_g = M$ in natural units. So alternatively we can write $\Delta = r^2 - 2r_gr + a^2$.
We can consider the simple case of a non-rotating black hole with $a = 0$. Then we get:

$$\Sigma = r^2 \qquad \Delta = r^2 - 2Mr = r^2 - 2r_gr$$

and (11) reduces to the Schwarzschild metric (4), as expected. [21]
In the last section we saw that the event horizon of the Schwarzschild black hole was located at $r = r_S$ where $g_{tt} \to 0$ and $g_{rr} \to \infty$. Looking at (11), we notice that these conditions do not occur in the same place. First of all $g_{tt} = 0$ can be obtained by solving the quadratic equation $(1 - \frac{2Mr}{\Sigma}) = 0$ and neglecting the negative solution:

$$r = r_E = r_g + \sqrt{r_g^2 - a^2cos^2\theta} = M + \sqrt{M^2 - a^2cos^2\theta}. \tag{12}$$

r_E is called the static limit. Inside r_E all observers must orbit the black hole in the direction in which the black hole rotates, i.e. they can not be static, which is due to the effect of frame-dragging ([24] p.879).

Similarly, the condition $g_{rr} \to \infty$ is met for $\Delta = 0$ at

$$r = r_H = r_g + \sqrt{r_g^2 - a^2} = M + \sqrt{M^2 - a^2}. \tag{13}$$

r_H is the actual black hole horizon. Just like with the Schwarzschild horizon, observers "can fall inward through it but can never emerge outward" ([24] p.879). The coordinate singularity that we encounter here can again be avoided by choosing different coordinates. A suitable set in this case are Kerr coordinates [34], which we will not further explore here. We can see that $r_H < r_E$ except at the poles ($\theta = 0$ and $\theta = \pi$, where $r_H = r_E$. At the equator ($\theta = \frac{\pi}{2}$), $r_E = 2r_g = r_S$ is exactly equal to the Schwarzschild radius.
The region $r_H < r < r_E$ between the static limit and the event horizon is called the

ergosphere, which we did not encounter in the Schwarzschild solution and is new for rotating black holes ([21] p. 236). We can plot the ergosphere for different values of a (see Fig. 7).

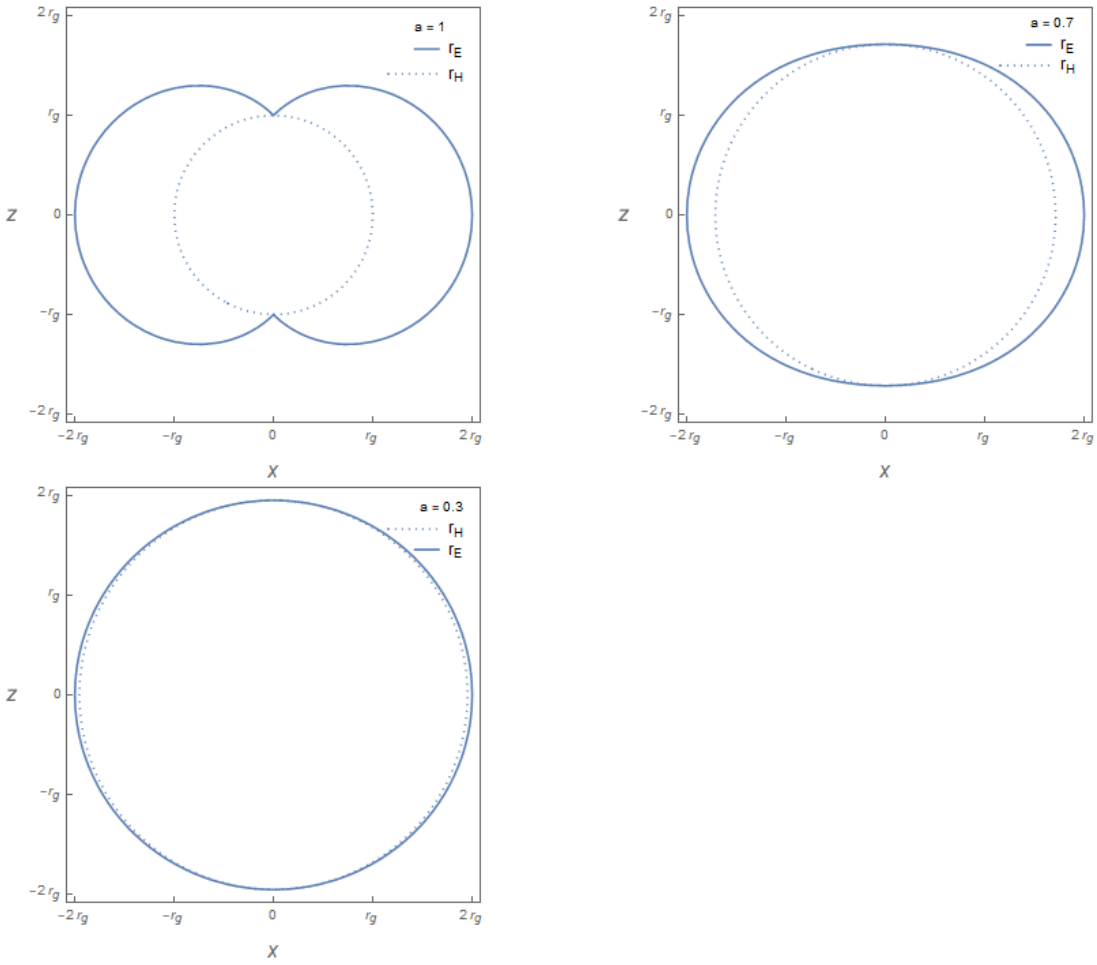

Figure 7: Plots of the black hole ergosphere
The static limit r_E and black hole horizon r_H for a rotating Kerr-black hole for different values of a. The ergosphere is the region between r_H and r_E.

Lastly, we can examine the symmetries of the Kerr solution. In Boyer-Lindquist coordinates the metric components are independent of t and φ, which gives rise to the Killing vectors

$$\frac{\partial}{\partial t} \qquad \text{and} \qquad \frac{\partial}{\partial \varphi} \tag{14}$$

as we have seen for the Schwarzschild metric.

2.2 Black Hole in a Uniform Magnetic Field - The Wald Solution

With the basic understanding of black holes in General Relativity, we can start to tackle Wald's solution for a black hole in a magnetic field. But before that we may want to ask ourselves one more thing:
"Where does the magnetic field around a black hole come from?"
To answer the question, we will follow the calculations in ([21] pp. 610-611). There the author discusses the magnetosphere of an 'isolated' (stellar) black hole. Starting point is the magnetic moment of strength on the horizon

$$\mu_H = \frac{QGM}{c^2} j, \tag{15}$$

where Q is the total charge on the black hole, M its mass and j a dimensionless rotational parameter used in [21] ($a = jr_g = jM$). On the other hand $\mu_H = B_H r_H^3$ and thus the magnetic field strength on the horizon is

$$B_H = 2.4 \cdot 10^{19}\,\mathrm{G}\,\frac{qj}{(1+\sqrt{1-j^2})^3}\,m^{-1} \tag{16}$$

and $q = Q/(5.14 \cdot 10^{29}\,\text{statcoulombs})\,m^{-1}$ is the total charge Q divided by the maximum amount possible.
In order to support a strong magnetic field, the black hole has to be charged significantly. But in realistic situations particle creation and plasma accretion interfere with the charged state. According to Blandford and Znajek, (Meier) claims, if a critical magnetic field strength of about $B_{crit} \approx 2.5 \cdot 10^5\,\mathrm{G}\,j^{\frac{1}{2}}m^{-\frac{1}{2}}$ is exceeded, electron-positron creation would quickly discharge the excess charges. Furthermore, this field strength is much smaller and negligible compared to the $10^8\,\mathrm{G} - 10^9\,\mathrm{G}$ fields produced by matter accretion (for supermassive black holes like M87* field strengths of about $10^4\,\mathrm{G}$ are common). Thus, in a realistic situation black holes have no significant intrinsic magnetic field due to them being charged. Instead, the field is supported by plasma currents in the vicinity of the black hole. "An appreciably magnetized black hole, therefore, is never truly isolated" ([21] p.609).
Wald himself addresses this in ([36] Sec. 1), where he explains that only charged (isolated) black holes can have an electromagnetic field, and therefore exhibit electromagnetic effects, while the electromagnetic fields of a black hole that is not isolated are due to 'external sources' like the surrounding plasma.
Wald's solution is a vacuum solution.

The situation in his paper is the following:
A stationary, axisymmetric black hole in vacuum is placed in an originally uniform magnetic test field of strength B_0, which is aligned with the black hole's rotational symmetry axis and no assumptions are made about the particular space-time metric. ([36] Sec. 1)

Starting point of the discussion is an arbitrary Killing vector ξ and Killing's equation (8). A Killing vector in a vacuum space-time is a solution of Maxwell's equations, because,

if one sets

$$F_{\mu\nu} = \xi_{\nu;\mu} - \xi_{\mu;\nu} \overset{(8)}{=} -2\xi_{\mu;\nu}, \tag{17}$$

then $F_{\mu\nu}$ satisfies the source-free Maxwell's equations

$$F^{\mu\nu}{}_{;\nu} = -2\xi^{\mu;\nu}{}_{;\nu} = 0. \tag{18}$$

As we have already seen with the Scharzschild metric and the Kerr metric, stationary and axisymmetric black holes possess the time-like Killing vector $\frac{\partial}{\partial t}$, here denoted as η^μ, and the axial Killing vector $\frac{\partial}{\partial \varphi}$, denoted as ψ^μ. Wald then considers the Maxwell test fields generated by these Killing vectors:

$$F_\psi = \boldsymbol{d}\psi \quad and \quad F_\eta = \boldsymbol{d}\eta, \tag{19}$$

where $\boldsymbol{d}$ denotes the exterior derivative. These test fields are both stationary and axially symmetric. F_ψ generates a uniform magnetic field, while F_η generates an electromagnetic field.

Now, in order to obtain the solution for the electromagnetic test field F in the case of a black hole being placed in a uniform magnetic field of strength B_0, which is aligned along the black hole's symmetry axis, F must satisfy the following:

- (I) F must be stationary and axisymmetric
- (II) F must be non-singular in the exterior region and on the black hole horizon
- (III) At large distances from the black hole, F must asymptotically approach a uniform magnetic field of strength B_0
- (IV) The charge and magnetic monopole moment of F must vanish

(I)-(IV) now uniquely determine the test field if one applies the following theorem, which is also quoted in [36] (see also [14]).

> Theorem: Let F be a Maxwell test field on a stationary, axisymmetric, vacuum black hole space-time. Suppose F satisfies the following properties:
>
> - (1) F is stationary and axisymmetric
> - (2) F must be non-singular in the exterior region and on the black hole horizon
> - (3) At large distances from the black hole, F vanishes
> - (4) F has no charge or magnetic monopole moment
>
> Then $F = 0$.

Finally, the field tensor which satisfies (I)-(IV) is given by:

$$F = \frac{1}{2}B_0\left(d\psi + \frac{2S}{M}d\eta\right). \tag{20}$$

Here, S is the black hole's angular momentum and M its mass. (20) is the Wald solution for an arbitrary stationary and axisymmetric vacuum-black-hole space-time in a uniform magnetic field. For the case of a Kerr black hole (11) with the tetrad of zero angular momentum observers (ZAMO)

$$\begin{aligned}
\omega^0 &= \left(\frac{\Delta}{\Sigma}\right)^{\frac{1}{2}}(dt - asin^2\theta d\varphi) \\
\omega^1 &= \left(\frac{\Sigma}{\Delta}\right)^{\frac{1}{2}} dr \\
\omega^2 &= \Sigma^{\frac{1}{2}} d\theta \\
\omega^3 &= \frac{sin\theta}{\Sigma^{\frac{1}{2}}}\big[(r^2+a^2)d\varphi - adt\big]
\end{aligned} \tag{21}$$

(20) becomes

$$\begin{aligned}
F =& B_0\left[\frac{arsin^2\theta}{\Sigma} - \frac{ma(r^2 - a^2cos^2\theta)(1+cos^2\theta)}{\Sigma^2}\right]\omega^1 \wedge \omega^0 \\
&+B_0\left[\frac{\Delta^{\frac{1}{2}} rsin\theta}{\Sigma}\right]\omega^1 \wedge \omega^3 + B_0\left[\frac{\Delta^{\frac{1}{2}} asin\theta cos\theta}{\Sigma}\right]\omega^2 \wedge \omega^0 \\
&+B_0\frac{cos\theta}{\Sigma}\left[r^2 + a^2 - \frac{2mra^2(1+cos^2\theta)}{\Sigma}\right]\omega^2 \wedge \omega^3.
\end{aligned} \tag{22}$$

(22) is a rather complicated expression in the exterior algebra of differential geometry. ([21] p.618) presents a more intuitive and familiar form of the magnetic field in Boyer-Lindquist coordinates, which depends on the metric tensor:

$$\begin{aligned}
B^r &= -\frac{B_0}{2\sqrt{g_{\theta\theta}g_{\varphi\varphi}}}\frac{\partial}{\partial\theta}\big(g_{\varphi\varphi} + 2ag_{t\varphi}\big) \\
B^\theta &= \frac{B_0}{2\sqrt{g_{rr}g_{\varphi\varphi}}}\frac{\partial}{\partial r}\big(g_{\varphi\varphi} + 2ag_{t\varphi}\big) \\
B^\varphi &= 0.
\end{aligned} \tag{23}$$

Similarly the electric field is given by

$$\begin{aligned}
E^r &= -\frac{B_0}{\sqrt{g_{rr}}}\frac{\partial}{\partial r}\big(g_{t\varphi} + 2ag_{tt}\big) \\
E^\theta &= -\frac{B_0}{\sqrt{g_{\theta\theta}}}\frac{\partial}{\partial\theta}\big(g_{t\varphi} + 2ag_{tt}\big) \\
E^\varphi &= 0.
\end{aligned} \tag{24}$$

Here, however, we will take a different approach and calculate the magnetic flux instead.

2.3 Calculation and Visualization of the Black Hole Magnetic Flux

In [7], the authors begin their discussion by considering the magnetic flux of a uniform external magnetic field, which is aligned with the black hole's rotation axis, through an imagined two-dimensional space-like Surface S around the black hole (see Fig. 8). Here, we will follow their approach but include more steps in finding the final equations.

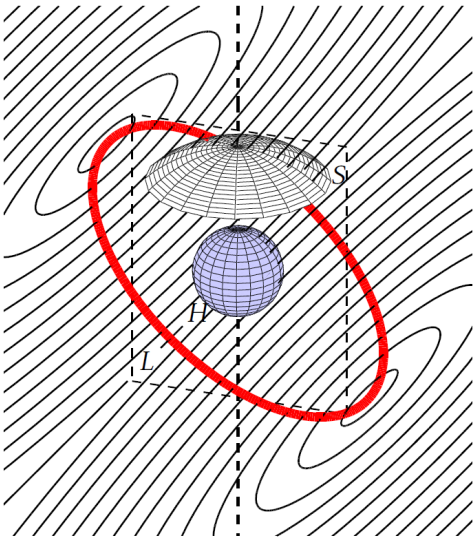

Figure 8: Flux geometry
The geometric situation considered in [7]. H represents the black hole horizon, the external magnetic field is generated by the current loop L and S is the surface area, across which the flux is measured.

The surface S can be thought of as part of a sphere with constant radius in spheroidal coordinates r, θ and φ. Now the magnetic flux across the surface can be expressed as

$$\Phi_m = \int_S F \wedge dS, \tag{25}$$

where F is the electromagnetic-field tensor from classical electrodynamics and dS stands for a surface element within the four-dimensional spacetime. (25) is reminiscent of the classical expression for the flux of any vector field $\vec{X}$ through a surface A: $\Phi = \int_A \vec{X}\, d\vec{A}$. Similarly, there is an expression for the electric flux:

$$\Phi_e = \int_S \star F \wedge dS, \tag{26}$$

where $\star F$ now denotes the Hodge-dual of the field tensor. Next, however, we will focus on the magnetic flux.

The authors state that, if S is part of an $r = const.$ sphere (25) can be simplified to

$$\Phi_m = \iint F_{\theta\varphi} d\theta d\varphi, \tag{27}$$

where $F_{\theta\varphi}$ can be thought of as the radial component of the magnetic field.
The final result for Φ_m is given in [7] as follows:

$$\Phi_m = \pi B_{\parallel} \left(\Delta + \frac{2Mr}{\Sigma}(r^2 - a^2) \right) sin^2\theta. \tag{28}$$

With the familiar abbreviations $\Delta = r^2 - 2Mr + a^2$ and $\Sigma = r^2 + a^2 cos^2\theta$. $B_{\parallel}$ is the component of the magnetic field, which is parallel to the black hole's rotation axis, as opposed to the component $B_{\perp}$ perpendicular to the axis. As stated above, for now we only consider the case where the external magnetic field is aligned with the rotation axis (i.e. $B_{\perp} = 0$) but we still distinguish the two components for clarity.

In order to obtain the result in (28), we have to calculate the component $F_{\theta\varphi}$ which can be done by using the well-known relation of electrodynamics between the electromagnetic-field-tensor F and the electromagnetic four-potential A (see Sec. 3.1):

$$F_{\mu\nu} = \frac{\partial A_\nu}{\partial x^\mu} - \frac{\partial A_\mu}{\partial x^\nu}. \tag{29}$$

The x^μ are the respective coordinates in use, here: $\{t, r, \theta, \varphi\}$. We can find a general expression for the A_μ in the appendix of [7] and they are covered in more detail in the appendix of [2]. Considering the special case $B_{\perp} = 0$ the components of the four-potential are as follows:

$$\begin{aligned}
A_t &= B_{\parallel} a \left[Mr \frac{(1 + cos^2\theta)}{\Sigma} - 1 \right] \\
A_r &= 0 \\
A_\theta &= 0 \\
A_\varphi &= B_{\parallel} \left[\frac{1}{2}(r^2 + a^2) - a^2 Mr \frac{(1 + cos^2\theta)}{\Sigma} \right] sin^2\theta.
\end{aligned}$$

According to (29), we can now calculate $F_{\theta\varphi}$ by simple derivation:

$$F_{\theta\varphi} = \frac{\partial A_\varphi}{\partial \theta} - \frac{\partial A_\theta}{\partial \varphi} = B_{\parallel} \underbrace{(r^2 + a^2 - 2Mr)}_{=\Delta} cos\theta sin\theta + 4B_{\parallel} Mr sin(2\theta) \frac{r^4 - a^4}{(a^2 + 2r^2 + a^2 cos(2\theta))^2}. \tag{30}$$

Consider the denominator in the second term of (30):

$$\begin{aligned}(a^2+2r^2+a^2\underbrace{cos(2\theta)}_{=cos^2\theta-sin^2\theta})^2 &= (a^2\underbrace{(1-sin^2\theta)}_{=cos^2\theta}+a^2cos^2\theta+2r^2)^2\\ &= (2a^2cos^2\theta+2r^2)^2\\ &= 4(r^2+a^2cos^2\theta)^2\\ &= 4\Sigma^2.\end{aligned}$$

Using the double angle formula $sin(2\theta) = 2sin\theta cos\theta$, we arrive at:

$$F_{\theta\varphi} = B_\parallel\left[\Delta+\frac{2Mr}{\Sigma^2}(r^4-a^4)\right]sin\theta cos\theta, \tag{31}$$

which is equal to the expression for $F_{\theta\varphi}$ given in [2].

Now we can finally proceed to calculate the magnetic flux

$$\begin{aligned}\Phi_m &= \underbrace{\int_0^{2\pi}d\varphi}_{=2\pi}\int_0^\theta F_{\theta'\varphi}d\theta'\\ &= 2\pi B_\parallel\left(-\frac{1}{2}\Delta cos^2\theta'+\frac{Mr}{a^2}\frac{r^4-a^4}{r^2+a^2cos^2\theta'}\right)\Bigg|_0^\theta\\ &= 2\pi B_\parallel\left(-\frac{1}{2}\Delta(cos^2\theta-1)+\frac{Mr}{a^2}(r^4-a^4)\underbrace{\left(\frac{1}{\Sigma}-\frac{1}{r^2+a^2}\right)}_{\frac{a^2sin^2\theta}{(r^2+a^2)\Sigma}}\right)\\ &= \pi B_\parallel\left(\Delta+\frac{2Mr}{\Sigma}(r^2-a^2)\right)sin^2\theta.\end{aligned} \tag{32}$$

This is exactly the expression in (28) and we have arrived at the same result as [7].
Now we can visualize the magnetic flux by plotting the different constant flux surfaces. To do this, we set $\Phi_m = const.$ and create an array of values. In Mathematica this can be done with the Table function.

```
data := Table[Pi*B0*Sin[ArcCos[z/Sqrt[x^2+z^2]]]^2
        (Sqrt[x^2+z^2]^2+a^2-2M*Sqrt[x^2+z^2]]
        +(2M*Sqrt[x^2+z^2])*(Sqrt[x^2+z^2]^2-a^2)/
        (Sqrt[x^2+z^2]^2+a^2*Cos[ArcCos[z/Sqrt[x^2+z^2]]]^2))==C,
        {C,1,300,35}]
```

We substitute in our expression for Φ_m and set it equal to a constant C, which here ranges from 1 to 300 in steps of 35. Notice that in order to plot the flux surfaces in the x-z-plane, we need to use the conversion rules of r and θ to the plane:

$$r = \sqrt{x^2 + z^2}$$
$$\theta = arccos\left(\frac{z}{\sqrt{x^2 + z^2}}\right)$$

For each of these values we can then make a parametric plot for the respective flux surface using Mathematica's ContourPlot in the desired x- and z-range like this:

```
ContourPlot[Evaluate[data], {x, -2 M, 2 M}, {z, -2 M, 2 M}].
```

And we obtain the final images.

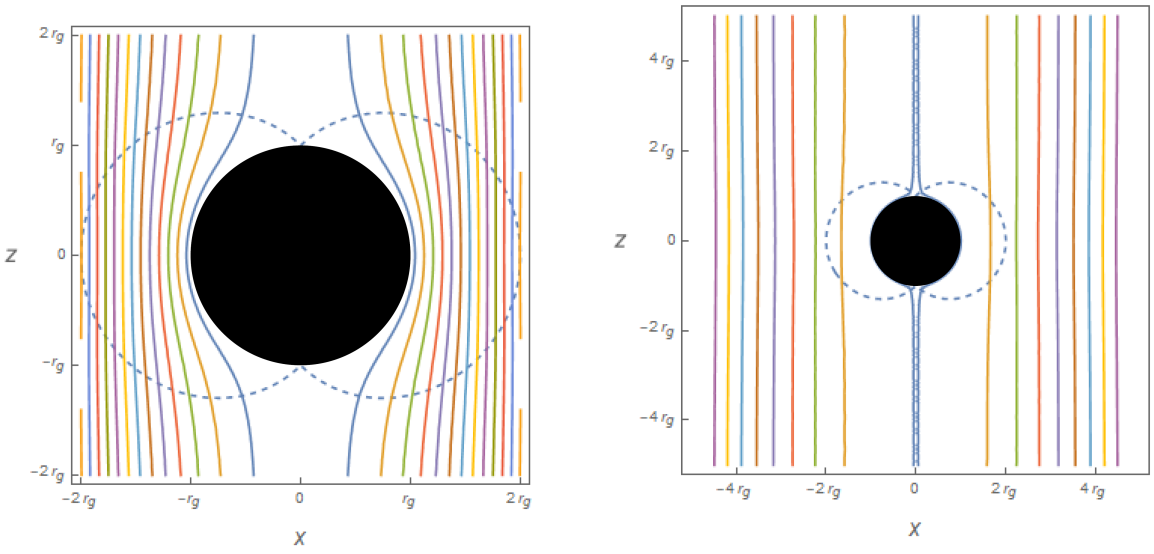

Figure 9: Magnetic flux surfaces near and far from the black hole for $a = 1$
Left: Near the horizon. Right: Further away from the horizon. The dashed line indicates the static limit.

We can see that for a non-rotating black hole the surfaces of constant flux simply penetrate the horizon (Fig.10), whereas the flux in case of fast rotation (Fig.9) is completely expelled from it. This is called the "Meissner effect" [22] known from solid state physics, because the black hole acts like a superconductor in this case.

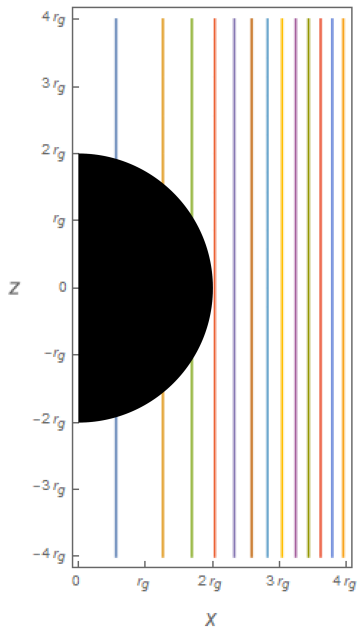

Figure 10: Magnetic flux surfaces near the black hole for $a = 0$

Let us take a moment and think about the flux surfaces. The flux is the number of field lines that penetrate a particular surface area perpendicularly. This means that the magnetic field lines lie in the constant flux surfaces (i.e. they are tangential), shown in figure 9-10.

Similarly to (22) where the corresponding electric field can be obtained by taking the dual of F, one can use (26) to calculate the electric flux and its constant flux surfaces. In [7] the electric lines of force induced by the black hole's rotation are plotted (see Fig.11-12).

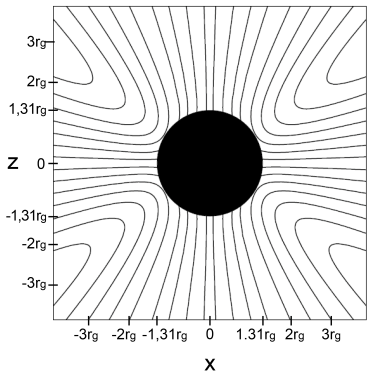

Figure 11: Electric field lines for $a = 0.95$. [7] (edited)

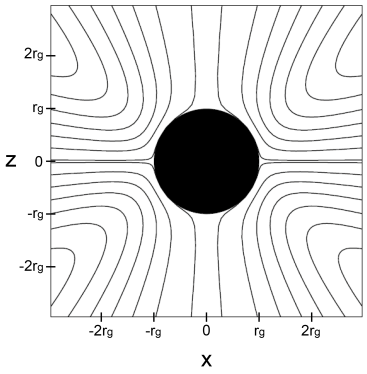

Figure 12: Electric field lines for $a = 1$. [7] (edited)

3 Electrodynamics and Radiation of Moving Charged Particles

Now before we begin our discussion of synchrotron radiation itself, let us take the same approach as in chapter 2 and first review some basics, now on the fields of *Special* Relativity and electrodynamics.

3.1 Special Relativity and Electrodynamics

The fundamental equations that describe all electromagnetic phenomena were found by James C. Maxwell. They have the form

$$\nabla \vec{E} = \frac{\rho}{\epsilon_0} \tag{33}$$

$$\nabla \times \vec{E} = -\frac{\partial \vec{B}}{\partial t} \tag{34}$$

$$\nabla \vec{B} = 0 \tag{35}$$

$$\nabla \times \vec{B} = \mu_0 \vec{j} + \epsilon_0 \mu_0 \frac{\partial \vec{E}}{\partial t}, \tag{36}$$

where $\vec{E}$ is the electric field, $\vec{B}$ the magnetic field, ρ the charge density and $\vec{j}$ is the electric current density. ϵ_0 and μ_0 represent the electric and magnetic field constants, respectively.
From these equations in vacuum ($\rho = 0$, $\vec{j} = 0$) one can easily derive the so-called wave equations for the electric and magnetic fields

$$\nabla^2 \vec{E} - \epsilon_0 \mu_0 \frac{\partial^2 \vec{E}}{\partial t^2} = 0 \qquad \text{and} \qquad \nabla^2 \vec{B} - \epsilon_0 \mu_0 \frac{\partial^2 \vec{B}}{\partial t^2} = 0, \tag{37}$$

which describe all forms of electromagnetic radiation. Compared to similar expressions of wave equations, one can see that the speed of light is given by $c = \frac{1}{\sqrt{\epsilon_0 \mu_0}}$. Besides, from the second and third of Maxwell's equations we can see that the magnetic and electric fields can be written in terms of a scalar potential Φ and a vector potential $\vec{A}$, such that

$$\vec{B} = \nabla \times \vec{A} \qquad \text{and} \qquad \vec{E} = -\nabla \Phi - \frac{\partial \vec{A}}{\partial t}. \tag{38}$$

This will turn out to be very useful later on.
The physics up to this point were mostly governed by Newtonian mechanics. Newtons laws were known to be invariant under Galilei transformations, for example when converting from a laboratory frame S into a frame S' that moves relative to it at a constant

velocity $\boldsymbol{v}$. In this case the Galileo transformation reads:

$$\vec{x'} = \vec{x} - \vec{v}t$$
$$t' = t.$$

Or in matrix form

$$\begin{pmatrix} t' \\ x' \\ y' \\ z' \end{pmatrix} = \begin{pmatrix} 1 & 0 & 0 & 0 \\ -v_x & 1 & 0 & 0 \\ -v_y & 0 & 1 & 0 \\ -v_z & 0 & 0 & 1 \end{pmatrix} \begin{pmatrix} t \\ x \\ y \\ z \end{pmatrix} \iff \begin{pmatrix} t' \\ \vec{x'} \end{pmatrix} = \begin{pmatrix} 1 & 0 \\ -\vec{v} & \mathbb{1} \end{pmatrix} \begin{pmatrix} t \\ \vec{x} \end{pmatrix} \tag{39}$$

So the time is treated like a universal parameter that is the same in all reference frames in Newtonian physics.
It quickly became apparent, however that Maxwell's equations are not invariant under Galilei transformations, giving rise to the theory of an ether that acts as a medium for the transport of light waves, just like sound waves need air as a transport medium. The ether theory was disproved by the Michelson-Morley experiment in 1887 [23]. Instead, Hendrik Anton Lorentz found a different kind of transformation that in fact do leave Maxwell's equations invariant. The approach is to assume an arbitrary linear transformation matrix and require form invariance of the resulting equations. A wonderful execution of this approach can be found in [13] (pp. 28-29).
Now the Lorentz transformation for motion in, say the x-direction ($\vec{v} = v\vec{e_x}$), can be written similarly to (39) but in order to circumvent the awkward first vector component, which has a different unit than the spatial components, we instead write ct, instead of simply t:

$$\begin{pmatrix} ct' \\ x' \end{pmatrix} = \gamma \begin{pmatrix} 1 & -\beta \\ -\beta & 1 \end{pmatrix} \begin{pmatrix} ct \\ x \end{pmatrix} \tag{40}$$

with the Lorentz factor $\gamma = (\sqrt{1-\beta^2})^{-1}$ and $\beta = \frac{v}{c}$. This is called a Lorentz boost.
For motion in an arbitrary direction, we can simply perform a rotation of the coordinate system in the direction of the velocity vector v, which is again given by a Lorentz transformation, with a subsequent Lorentz boost in this direction.
The tedious matrix notation can be replaced with a tensorial notation for the different objects, in which we no longer need the explicit matrix representation, in conjunction with Einstein's sum convention. With this (40) simply becomes

$$x'^{\mu} = \Lambda^{\mu}{}_{\nu}\, x^{\nu}, \tag{41}$$

where $\mu, \nu = 0, 1, 2, 3$ select the different components from the four-vector

$$\boldsymbol{x} = \begin{pmatrix} x^0 \\ x^1 \\ x^2 \\ x^3 \end{pmatrix} = \begin{pmatrix} ct \\ \vec{x} \end{pmatrix}, \tag{42}$$

which is called an event in the 3+1-dimensional spacetime. Here, we will denote regular 3-dimensional vectors with an arrow, while four-vectors are bold. The $\Lambda^{\mu}{}_{\nu}$ correspond to the components of the Lorentz transformation matrix Λ.
The events make up the 4-dimensional Minkowski space, which is central to Einstein's theory of Special Relativity. The Minkowski space is a 4-dimensional vector space equipped with a pseudo-scalar product, the Minkowski metric

$$\eta_{\mu\nu} = \begin{pmatrix} -1 & 0 & 0 & 0 \\ 0 & 1 & 0 & 0 \\ 0 & 0 & 1 & 0 \\ 0 & 0 & 0 & 1 \end{pmatrix}. \tag{43}$$

It is called a pseudo-scalar product (pseudo-metric) because it violates the requirement to be positive-definite, i.e. in Minkowski space it is possible for a vector, which is not the null vector, to have zero length:

$$\eta(\boldsymbol{x}, \boldsymbol{x}) = \eta_{\mu\nu} x^{\mu} x^{\nu} = x_{\mu} x^{\mu} = -c^2 t^2 + x^2 + y^2 + z^2 = 0. \tag{44}$$

This can be illustrated by a spacetime diagram, where all vectors that satisfy (44) lie on the so called light cone (see Fig.13). If the 'length' of an event is less than 0, it is called time-like, otherwise space-like. The spacetime diagram divides the history of an event into future and past.

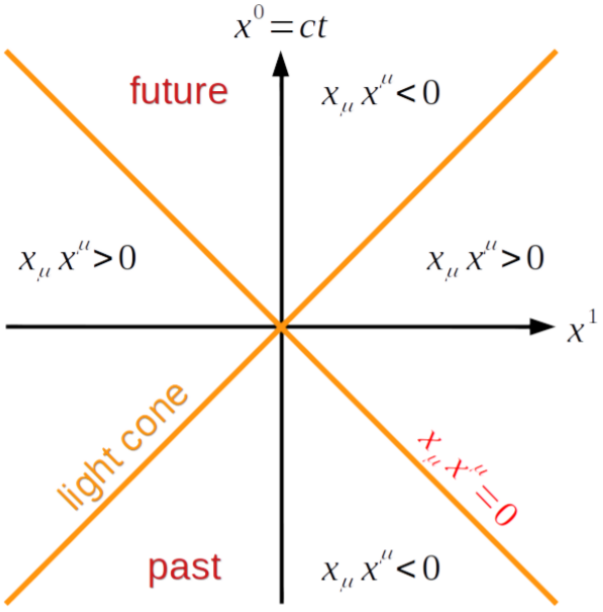

Figure 13: Spacetime diagram
A two-dimensional representation of a spacetime diagram. The x^1-axis really is the $\mathbb{R}^3$. Events that satisfy (44) lie on the light cone. [13] (p. 38)

Besides the 'position' four-vector $\boldsymbol{x}$ there are several other interesting four-vectors, similar to the dynamics in Newtonian physics. The four-velocity $\boldsymbol{u}$ of a particle can be defined by

$$\boldsymbol{u} = \dot{\boldsymbol{x}} = \frac{d\boldsymbol{u}}{d\tau} = \gamma \begin{pmatrix} c \\ \vec{v} \end{pmatrix}, \tag{45}$$

where τ is called the proper time, the time which is displayed by a clock attached to the particle's rest frame, where $\vec{v} = \vec{0}$. τ and t are related via $t = \gamma\tau$ Since massive particles can only move at speeds less than c, its trajectory through spacetime, the world line, is confined to the interior of the light-cone. In the proper time parameterization of a world line, we have ([13] p. 52)

$$u_\mu u^\mu = -c^2. \tag{46}$$

Next there is the four-momentum $\boldsymbol{p}$

$$\boldsymbol{p} = m\boldsymbol{u} = \gamma m \begin{pmatrix} c \\ \vec{v} \end{pmatrix} = \begin{pmatrix} \frac{E}{c} \\ \vec{p} \end{pmatrix}, \tag{47}$$

where m is the particles rest mass. With (46) we can see that

$$p_\mu p^\mu = m^2 u_\mu u^\mu = -m^2 c^2. \tag{48}$$

But on the other hand (47) yields

$$p_\mu p^\mu = -\frac{E^2}{c^2} + p^2, \tag{49}$$

where $p = |\vec{p}|$. In summary, we arrive at the important relativistic energy-momentum relation

$$E^2 = m^2 c^4 + p^2 c^2. \tag{50}$$

Finally, the four-acceleration is defined by

$$\boldsymbol{a} = \frac{d\boldsymbol{u}}{d\tau} \tag{51}$$

and this lets us define the four-force

$$\boldsymbol{f} = m\boldsymbol{a} = \frac{d\boldsymbol{p}}{d\tau} \tag{52}$$

Before we discuss the relativistic four-force in electrodynamics in more detail, let us shift gears for a moment and remember the scalar and vector potentials Φ and $\vec{A}$ from (38) that helped us rewrite the electric and magnetic fields. We can define the four-potential

$$A^\mu = \begin{pmatrix} \frac{\Phi}{c} \\ \vec{A} \end{pmatrix} \tag{53}$$

and the gradient operator

$$\partial_\mu = \begin{pmatrix} \frac{1}{c}\partial_t & \nabla \end{pmatrix} \tag{54}$$

to obtain the anti-symmetric electromagnetic field tensor

$$F_{\mu\nu} = \partial_\mu A_\nu - \partial_\nu A_\mu, \tag{55}$$

which contains the whole information about the fields $\vec{E}$ and $\vec{B}$. If we explicitly calculate the components $F_{\mu\nu}$, we find

$$F_{\mu\nu} = \begin{pmatrix} 0 & -\frac{E_x}{c} & -\frac{E_y}{c} & -\frac{E_z}{c} \\ \frac{E_x}{c} & 0 & B_z & -B_y \\ \frac{E_y}{c} & -B_z & 0 & B_x \\ \frac{E_z}{c} & B_y & -B_x & 0 \end{pmatrix} \tag{56}$$

With that, we can study the expression for the electromagnetic force ([13] p. 61)

$$\frac{dp^\mu}{d\tau} = qF^{\mu\nu}u_\nu, \tag{57}$$

where q is the particle's charge and we get the field tensor with upper indices via contraction with the metric tensor $F^{\mu\nu} = \eta^{\mu\alpha}\eta^{\nu\beta}F_{\alpha\beta}$. For $\mu = 1, 2, 3$ we can recover the respective components for the familiar form of the Lorentz force

$$\frac{d\boldsymbol{p}}{d\tau} = q\gamma(\vec{E} + \vec{v} \times \vec{B}) \tag{58}$$

and in coordinate time t

$$\frac{d\boldsymbol{p}}{dt} = q(\vec{E} + \vec{v} \times \vec{B}) \tag{59}$$

where here $\boldsymbol{p} = \gamma m\vec{v}$ is the spatial three-vector because we used $\mu = 1, 2, 3$.

3.2 Synchrotron Radiation

After the quick review of relativistic dynamics at the end of the last section, it is time to focus on synchrotron radiation itself.
Synchrotron radiation is produced when a relativistic, charged particle is accelerated by a magnetic field. If we consider only a magnetic field $\vec{B}$ for the force in (57), we obtain the equations ([31] pp. 167-168)

$$\frac{d}{dt}(\gamma mc^2) = q\vec{E}\vec{v} = 0 \quad \text{for } \mu = 0 \tag{60}$$

$$\frac{d}{dt}(\gamma m\vec{v}) = \frac{q}{c}\vec{v} \times \vec{B} \quad \text{for } \mu = 1, 2, 3. \tag{61}$$

From the second equation we see that

$$\gamma m \frac{d\vec{v}}{dt} = \frac{q}{c}\vec{v} \times \vec{B}. \tag{62}$$

If we write $\vec{v} = \vec{v}_\perp + \vec{v}_\parallel$ as a sum of the parts perpendicular and parallel to $\vec{B}$, we get

$$\frac{d\vec{v}_\parallel}{dt} = 0 \qquad \text{and} \qquad \frac{d\vec{v}_\perp}{dt} = \frac{q}{\gamma mc}\vec{v}_\perp \times \vec{B} = \underbrace{\frac{qB}{\gamma mc}}_{\Omega} v_\perp, \tag{63}$$

so the particle is forced into a rotation with a frequency Ω. Since the component parallel to $\vec{B}$ does not get affected, this results in a helical motion. As we know from classical electrodynamics, accelerated charges produce radiation. This fact is expressed by the well-known Larmor formula, which describes the total energy loss in the form of the emitted power P_{em}^{tot} of a particle with charge q that is subject to an acceleration $\vec{a}$ in the non-relativistic limit

$$P_{em}^{tot} = -\frac{dE}{dt} = \frac{q^2\vec{a}^2}{6\pi c^3 \epsilon_0} = \frac{2q^2\vec{a}^2}{3c^3}, \tag{64}$$

where the term after the second equal sign is in cgs-units, where $\epsilon_0 = 4\pi$. In section 4.1 of [5] this expression is converted into a covariant form, which reduces to (64) again in a frame, in which the particle is non-relativistic. With that one obtains an expression that is also valid for relativistic speeds, if Lorentz transformed into a frame where the particle is relativistic. According to (52) a proper expression, which reduces to $\vec{a}^2$ in the non-relativistic limit is

$$\frac{1}{m^2}\frac{dp_\mu}{d\tau}\frac{dp_\mu}{d\tau}. \tag{65}$$

With that and the expression for the force (57) for a magnetic field $\vec{B}$ aligned with the z-axis one eventually obtains

$$P_{em}^{tot} = -\frac{dE}{dt} = \frac{2q^4}{3m^2c^3}\gamma^2 B^2 v^2 sin^2\alpha, \tag{66}$$

where the pitch angle α is the angle between $\vec{B}$ and the particle's velocity $\vec{v}$. Due to the m^{-2}-dependency, particles with large mass are negligible and only electrons (positrons) are considered to contribute to the synchrotron process ([38] p.6).
One can then calculate the emitted synchrotron radiation spectrum $P_{em}(\nu)$ of a particle (electron). A detailed derivation is given in Sec. 4.2-4.3 of [5].

$$P_{em}(\nu) = \frac{\sqrt{3}e^3 B sin\alpha}{mc^2} \underbrace{\frac{\nu}{\nu_c}\int_{\frac{\nu}{\nu_c}}^{\infty} d\xi K_{\frac{5}{3}}(\xi)}_{F(n)} = \frac{\sqrt{3}e^3 B}{mc^2} F(n) sin\alpha \tag{67}$$

with the critical frequency $\nu_c = (3eB\gamma^2)/(4\pi mc)sin\alpha$, the modified Bessel function of order $5/3$ $K_{5/3}$ and $n = \nu/\nu_c$.

4 Synchrotron Radiation in Wald's Magnetic Field

Now that we have studied both the pitch angle dependency of the synchrotron radiation and Wald's solution for the black hole magnetosphere, we can start to develop our model to explain the circular emission ring and the black hole shadow of M87*.
We consider electrons that are accelerated to relativistic speeds inside the jet moving, in the simplest case, parallel to the black hole's rotation axis (z-axis in Fig. 9) slightly above the black hole horizon at $z \approx> r_g$. As we have already discussed in section 2.3, the magnetic field lines are at all points tangential to the surfaces of constant flux depicted in Fig. 9. This means that the electrons, moving in the black hole magnetosphere, as described by Wald's solution are subject to a Lorentz force in those regions, where the field lines are curved around the black hole. The pitch angle dependency leads to anisotropic synchrotron radiation, as we will explain in what follows.
Close to the rotation axis ($x = 0$) and further out ($x \approx> 2r_g$) we do not expect any synchrotron emissions, because in these areas we have a pitch angle of $\alpha = 0$ and, thus, no Lorentz force acts on the electrons.
Contrarily, in the region $r_g <\approx z$, where the field lines are sufficiently bent and $\alpha > 0$ there will be synchrotron emission. According to the right-hand-rule a force will act on the electrons, whose direction will point in the negative y-direction, i.e. into the paper plane for $x > 0$ and in the positive y-direction for $x < 0$.
Since the flux surfaces in figures 9-10 are cross sections that possess rotational symmetry around the z-axis, the electrons will perform a circular motion around the z-axis. In other words, for a fixed coordinate $z = const. \approx> r_g$ the pitch angle α, and therefore the emitted synchrotron power P_{em} first increase, when moving radially outward, then reach a maximum, where α becomes maximal, and finally decreases again because the field of Wald's solution approaches a uniform magnetic field.
We can calculate $\alpha = \alpha(x)$ as a function of the spatial coordinate x. To do this, we interpret the magnetic flux surfaces, described by (32) as a scalar field $\Phi_m(x, z)$ and consider its gradient vector at the positions $(x; z = const.)$. We can calculate the angle between this vector and the unit vector in z-direction $\vec{z}$.
This can be done with the function VectorAngle in Mathematica. Since we want the angle between the tangent to the surface and $\vec{z}$ and not between the surface normal (gradient) and $\vec{z}$, we have to subtract the angle from $\pi/2$

$$\alpha(x) = \frac{\pi}{2} - \text{VectorAngle}\big[grad(\Phi_m(x, z)), \{0, 1\}\big]. \tag{68}$$

The emitted synchrotron power in (67) essentially depends on $sin(\alpha(x))$, scaled by a factor, which depends on ν/ν_c.
Plotting $sin(\alpha(x))$ for $z = 1.1$ and $a = 1$, we get figure 14. Surprisingly, we obtain negative values shortly behind $2\,r_g$ and then the curve approaches 0. This means the angle between the gradient and the $\vec{z}$-direction becomes slightly greater than $\frac{\pi}{2} = 90°$. We assume this is due to numerical uncertainties in the complicated expression of $\alpha(x)$. However, the values there are very small and the asymptotic behaviour at 0 and infinity

is still correct. If we consider the total emitted radiation in (66), which depends on $sin^2\alpha(x)$, this does not play any role at all.

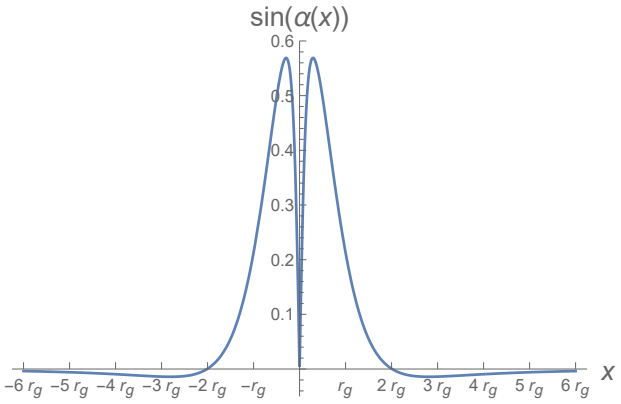

Figure 14: Pitch angle dependency
of the emitted synchrotron power in Wald's solution.

The synchrotron emission peaks at about $x = 0.2\, r_g$ from the rotation axis, until it ceases at approximately $x \approx> 2\, r_g$.
If we rotate Fig. 14 around its axis to obtain a surface of revolution and color code the height, we can create a 'from-top'-view of the emitted synchrotron radiation (Fig. 15). Where red/yellow means high/moderate emission and white/blue means low/no emission.

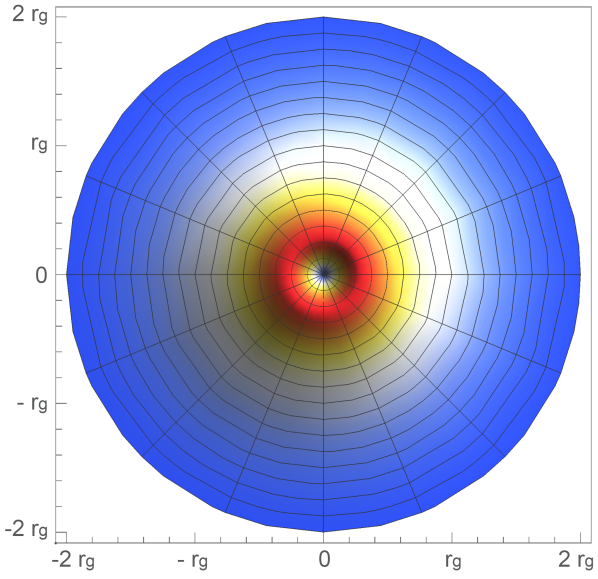

Figure 15: From-top-view of the synchrotron emission.
The emission has the morphology of a ring.

The asymmetry of the ring can still be attributed to Doppler beaming and the 17° tilt of the jet axis. In our plots this effect was neglected, however.
The lack of synchrotron emission close to the rotation axis and at larger distances together with the synchrotron emission inside a certain region in between can, thus explain the ring morphology of the emission around M87.

5 Conclusion

Throughout the course of this thesis we have discussed the active galaxy M87 and its properties. We have taken a glimpse at the EHT collaboration and their astounding work, which led to the first direct evidence for the existence of black holes. According to the EHT scientists the image of M87* shows the black hole shadow surrounded by a bright emission ring, which is due to the black hole's photon sphere. The asymmetric appearance of the ring can be attributed to the effect of relativistic Doppler beaming.
To develop our alternative explanation for the emission ring, we have reviewed some basics of Einstein's Special and General Theory of Relativity, which gave us a better understanding for the parts we needed for our model.
General Relativity led us to the description of the magnetosphere of a rotating Kerr black hole by Wald's solution, for which we calculated and visualized the constant flux surfaces. With Special Relativity, we examined the synchrotron radiation of electrons and how the emitted power depends on the pitch angle α between the magnetic field $\vec{B}$ and the particle's velocity $\vec{v}$.
By combining these two pieces, we were able to plot the pitch angle $\alpha(x)$, depending on the spatial distance x from the rotation axis and explain the ring-like appearance of the emission region around M87* via anisotropic synchrotron emission by relativistic electrons in the black hole magnetic field, as described by Wald's solution.
However, there are several points our simple model is missing and that are worth exploring more deeply. For example, we only considered the Lorentz force on electrons due to the magnetic field but there is also a linear component in the formula that accelerates them along the electric field $\vec{E}$, which leads to additional radiation. This is the case for example in plasma-filled solutions. [16].
Wald's solution is a good approximation when the accretion rate is low, which is the case in M87 (see. Sec. 1.1) and the magnetic field is mainly the field advected with the accretion flow and the amount of excess charges does not suffice to short the electric field via electric currents.
Generally, however, sophisticated general relativistic magneto-hydrodynamic (GRMHD) simulations are the state-of-the-art technique to tackle these problems. [11] [20] Further study on the approach we took in this thesis to explain the emission ring of M87 could lead to deeper insight into the physics of extragalactic jets. [25] [32]

References

[1] K. Akiyama et al. "First M87 Event Horizon Telescope Results. I. The Shadow of the Supermassive Black Hole". In: *The Astrophysical Journal* 875.1 (2019), p. L1. DOI: 10.3847/2041-8213/ab0ec7. arXiv: 1906.11238 [astro-ph.GA].

[2] J. Bicak and V. Janis. "Magnetic fluxes across black holes". In: *Monthly Notices of the Royal Astronomical Society* 212 (Feb. 1985), pp. 899–915. DOI: 10.1093/mnras/212.4.899.

[3] R. D. Blandford and D. G. Payne. "Hydromagnetic flows from accretion disks and the production of radio jets." In: *Monthly Notices of the Royal Astronomical Society* 199 (June 1982), pp. 883–903. DOI: 10.1093/mnras/199.4.883.

[4] R. D. Blandford and R. L. Znajek. "Electromagnetic extraction of energy from Kerr black holes." In: *Monthly Notices of the Royal Astronomical Society* 179 (May 1977), pp. 433–456. DOI: 10.1093/mnras/179.3.433.

[5] G. R. Blumenthal and R. J Gould. "Bremsstrahlung, Synchrotron Radiation, and Compton Scattering of High-Energy Electrons Traversing Dilute Gases". In: *Reviews of Modern Physics* 42 (2 Apr. 1970), pp. 237–270. DOI: 10.1103/RevModPhys.42.237.

[6] S. Britzen and A. Müller. "Das erste Foto eines Schwarzen Lochs". In: *Sterne und Weltraum* 6 (June 2019), p. 30.

[7] Z. Budinova et al. "Magnetic fields around black holes". In: *European Journal of Physics* 21 (June 2000). DOI: 10.1088/0143-0807/21/4/304.

[8] EHT Collaboration. *Event Horizon Telescope*. URL: eventhorizontelescope.org (visited on 04/18/2020).

[9] Event Horizon Telescope Collaboration et al. "First M87 Event Horizon Telescope Results. IV. Imaging the Central Supermassive Black Hole". In: *The Astrophysical Journal* 875.1, L4 (Apr. 2019), p. L4. DOI: 10.3847/2041-8213/ab0e85. arXiv: 1906.11241 [astro-ph.GA].

[10] Event Horizon Telescope Collaboration et al. "First M87 Event Horizon Telescope Results. V. Physical Origin of the Asymmetric Ring". In: *The Astrophysical Journal* 875.1, L5 (Apr. 2019), p. L5. DOI: 10.3847/2041-8213/ab0f43. arXiv: 1906.11242 [astro-ph.GA].

[11] C. F. Gammie, J. C. McKinney, and G. Tóth. "HARM: A Numerical Scheme for General Relativistic Magnetohydrodynamics". In: *The Astrophysical Journal* 589.1 (May 2003), pp. 444–457. DOI: 10.1086/374594. arXiv: astro-ph/0301509 [astro-ph].

[12] H. Hinrichsen. *General Relativity: Lecture Notes*. 2020. URL: http://teaching.hayehinrichsen.de/lecturenotes/gr.pdf (visited on 04/18/2020).

[13] H. Hinrichsen. *Special Relativity and Classical Field Theory: Lecture Notes*. 2020. URL: http://teaching.hayehinrichsen.de/lecturenotes/sr.pdf (visited on 04/18/2020).

[14] J. R. Ipser. "Electromagnetic Test Fields Around a Kerr-Metric Black Hole". In: *Phys. Rev. Lett.* 27 (8 Aug. 1971), pp. 529–531. DOI: 10.1103/PhysRevLett.27.529.

[15] E. J. D. Jolley and Z. Kuncic. "Jet-driven disk accretion in low luminosity AGN?" In: *Astrophysics and Space Science* 310.3-4 (Aug. 2007), pp. 327–332. DOI: 10.1007/s10509-007-9543-3. arXiv: 0706.0763 [astro-ph].

[16] S. S. Komissarov and J. C. McKinney. "The 'Meissner effect' and the Blandford-Znajek mechanism in conductive black hole magnetospheres". In: *Monthly Notices of the Royal Astronomical Society* 377.1 (May 2007), pp. L49–L53. DOI: 10.1111/j.1745-3933.2007.00301.x. arXiv: astro-ph/0702269 [astro-ph].

[17] A. Levinson and F. Rieger. "Variable TeV Emission as a Manifestation of Jet Formation in M87?" In: *The Astrophysical Journal* 730.2, 123 (Apr. 2011), p. 123. DOI: 10.1088/0004-637X/730/2/123. arXiv: 1011.5319 [astro-ph.HE].

[18] M. Lucchini, F. Krauß, and S. Markoff. "The unique case of the AGN core of M87: a misaligned low power blazar?" In: *Monthly Notices of the Royal Astronomical Society* (Aug. 2019). ISSN: 1365-2966. DOI: 10.1093/mnras/stz2125.

[19] J. -P. Luminet. "Image of a spherical black hole with thin accretion disk." In: *Astronomy & Astrophysics* 75 (May 1979), pp. 228–235.

[20] J. C. McKinney and R. D. Blandford. "Stability of relativistic jets from rotating, accreting black holes via fully three-dimensional magnetohydrodynamic simulations". In: *Monthly Notices of the Royal Astronomical Society* 394.1 (Mar. 2009), pp. L126–L130. DOI: 10.1111/j.1745-3933.2009.00625.x. arXiv: 0812.1060 [astro-ph].

[21] D. L. Meier. *Black Hole Astrophysics: The Engine Paradigm*. Springer, 2012.

[22] W. Meissner and R. Ochsenfeld. "Ein neuer Effekt bei Eintritt der Supraleitfähigkeit". In: *Naturwissenschaften* 21.44 (Nov. 1933), pp. 787–788. DOI: 10.1007/BF01504252.

[23] A. A. Michelson and E. W. Morley. "On the Relative Motion of the Earth and of the Luminiferous Ether". In: *Sidereal Messenger* 6 (Nov. 1887), pp. 306–310.

[24] C. W. Misner, K. S. Thorne, and J. A. Wheeler. *Gravitation*. W. H. Freeman and Company, 1973.

[25] K. Nalewajko, M. Sikora, and A. Różańska. "Orientation of the crescent image of M 87*". In: *Astronomy & Astrophysics* 634 (Feb. 2020), A38. ISSN: 1432-0746. DOI: 10.1051/0004-6361/201936586.

[26] NASA. *An infrared/visible composite picture of the elliptical galaxy M87*. URL: https://www.nasa.gov/feature/goddard/2017/messier-87 (visited on 04/18/2020).

[27] ned.ipac.caltech.edu. *Kellermann Lecture Notes*. URL: https://ned.ipac.caltech.edu/level5/Sept04/Kellermann2/Kellermann3_7.html (visited on 04/18/2020).

[28] Messier Objects. URL: https://www.messier-objects.com/messier-87-virgo-a/ (visited on 04/18/2020).

[29] V. Perlick. *Gravitational Lensing*. URL: https://www.zarm.uni-bremen.de/fileadmin/user_upload/space_science/gravitational_theory/gravlens.pdf (visited on 04/18/2020).

[30] ResearchGate. *The anatomy of an AGN as according to the standard unified model. Figure from Urry & Padovani (1995)*. URL: https://www.researchgate.net/figure/The-anatomy-of-an-AGN-as-according-to-the-standard-unified-model-Figure-from-Urry_fig2_269116761 (visited on 04/18/2020).

[31] G. B. Rybicki and A. P. Lightman. *Radiative Processes In Astrophysics*. Weinheim: Wiley-VCH Verlag, 2004.

[32] E. Sobacchi and Y. E. Lyubarsky. "On the magnetization and the radiative efficiency of BL Lac jets". In: *Monthly Notices of the Royal Astronomical Society* 484.1 (Mar. 2019), pp. 1192–1201. DOI: 10.1093/mnras/stz044. arXiv: 1812.11435 [astro-ph.HE].

[33] A. Tursunov et al. *Supermassive black holes as possible sources of ultra high energy cosmic rays*. 2020. arXiv: 2004.07907 [astro-ph.HE].

[34] M. Visser. *The Kerr spacetime: A brief introduction*. 2007. arXiv: 0706.0622 [gr-qc].

[35] S. M. Wagh, S. V. Dhurandhar, and N. Dadhich. "Revival of the Penrose Process for Astrophysical Applications". In: *The Astrophysical Journal* 290 (Mar. 1985), p. 12. DOI: 10.1086/162952.

[36] R. M. Wald. "Black hole in a uniform magnetic field". In: *Physical Review D* 10 (6 Sept. 1974), pp. 1680–1685. DOI: 10.1103/PhysRevD.10.1680.

[37] R. C. Walker et al. "The Structure and Dynamics of the Subparsec Jet in M87 Based on 50 VLBA Observations over 17 Years at 43 GHz". In: *The Astrophysical Journal* 855.2 (Mar. 2018), p. 128. ISSN: 1538-4357. DOI: 10.3847/1538-4357/aaafcc.

[38] J. Wilms. *Astrophysics from Space: Lecture Slides*. URL: https://pulsar.sternwarte.uni-erlangen.de/wilms/teach/astrospace/spacechap6.pdf (visited on 04/18/2020).

Acknowledgements

I would like to thank Prof. Dr. Karl Mannheim for supervising this thesis and for many hours of discussions and patient explanations. He always provided me with helpful advice and took his time for my questions.
Furthermore, I want to thank the professors and tutors at the department of physics at the University of Würzburg for their excellent teaching that enabled me to write this thesis.
I thank my peer students and friends Roman Iotov, Moritz Schnelke and especially Patrick Kloster and Henri Scheppach, whom I can always ask for their advice and help.
Dear thanks to Alena Kollmann for many hours spent kindly helping me edit my plots and for her support and love.
Finally, my gratitude goes to my parents Regina and Karl-Heinz Kinadeter for raising me and their unconditional support, be it financially, educationally or intellectually.

Eidesstattliche Erklärung

Hiermit versichere ich, die vorliegende Arbeit selbstständig verfasst und keine anderen als die angegebenen Quellen und Hilfsmittel benutzt sowie die Zitate deutlich kenntlich gemacht zu haben.
Ich erkläre weiterhin, dass die vorliegende Arbeit in gleicher oder ähnlicher Form noch nicht im Rahmen eines anderen Prüfungsverfahrens eingereicht wurde.

Würzburg, den 9. Juli 2020 Raoul Emanuel Kinadeter